In vivo multifunctional optical coherence tomography at the periphery of the lungs

Feroldi, Fabio; Willemse, Joy; Davidoiu, Valentina; Gräfe, Maximilian G. O.; van Iperen, Dirck J.; Goorsenberg, Annika W. M.; Annema, Jouke T.; Daniels, Johannes M. A.; Bonta, Peter I.; de Boer, Johannes F.

published in
Biomedical Optics Express
2019

DOI (link to publisher)
10.1364/boe.10.003070

document version
Publisher's PDF, also known as Version of record

Research Article | Vol. 10, No. 6 | 1 Jun 2019 | BIOMEDICAL OPTICS EXPRESS 3070
Biomedical Optics EXPRESS

In vivo multifunctional optical coherence tomography at the periphery of the lungs

FABIO FEROLDI,[1] JOY WILLEMSE,[1,4] VALENTINA DAVIDOIU,[1,4] MAXIMILIAN G. O. GRÄFE,[1] DIRCK J. VAN IPEREN,[1] ANNIKA W. M. GOORSENBERG,[2] JOUKE T. ANNEMA,[2] JOHANNES M. A. DANIELS,[3] PETER I. BONTA,[2] AND JOHANNES F. DE BOER[1,*]

[1]*LaserLaB Amsterdam and Department of Physics and Astronomy, VU University Amsterdam, de Boelelaan 1081, 1081HV, Amsterdam, the Netherlands*
[2]*Amsterdam University Medical Center, Department of Pulmonology, University of Amsterdam, Amsterdam, the Netherlands*
[3]*Amsterdam University Medical Center, Department of Pulmonology, VUmc Location, Amsterdam, the Netherlands*
[4]*These authors contributed equally*
**jfdeboer@few.vu.nl*

Abstract: Remodeling of tissue, such as airway smooth muscle (ASM) and extracellular matrix, is considered a key feature of airways disease. No clinically accepted diagnostic method is currently available to assess airway remodeling or the effect of treatment modalities such as bronchial thermoplasty in asthma, other than invasive airway biopsies. Optical coherence tomography (OCT) generates cross-sectional, near-histological images of airway segments and enables identification and quantification of airway wall layers based on light scattering properties only. In this study, we used a custom motorized OCT probe that combines standard and polarization sensitive OCT (PS-OCT) to visualize birefringent tissue *in vivo* in the airway wall of a patient with severe asthma in a minimally invasive manner. We used optic axis uniformity (OAxU) to highlight the presence of uniformly arranged fiber-like tissue, helping visualizing the abundance of ASM and connective tissue structures. Attenuation coefficient images of the airways are presented for the first time, showing superior architectural contrast compared to standard OCT images. A novel segmentation algorithm was developed to detect the surface of the endoscope sheath and the surface of the tissue. PS-OCT is an innovative imaging technique that holds promise to assess airway remodeling including ASM and connective tissue in a minimally invasive, real-time manner.

1. Introduction

Over the past two decades, optical coherence tomography (OCT) has become a widely adopted optical imaging technique in ophthalmology, cardiology, gastroenterology, and dermatology [1]. Interventional pulmonology has not yet experienced widespread adoption of the technique. Several experimental research groups have demonstrated imaging of the airways in a clinical setting with small to medium-size cohorts. In particular, OCT has been used to investigate lung cancer [2–5], which is revealed in OCT images by the loss of the usual layered structure of the airway wall. Long-ranging anatomic-OCT has been developed to measure the diameter of the upper airways and assess respiratory issues such as sleep apnea [6–8]. OCT has attracted particular interest for the study of airway wall remodeling which is a crucial feature of chronic airway diseases [9,10]. Notably, Adams *et al.* showed that polarization-sensitive OCT (PS-OCT) can reveal the presence of airway smooth muscle (ASM) in the airway wall, suggesting that it may be a valuable tool for assessing tissue remodeling in asthma patients [11,12]. Other studies augmented the imaging capabilities of OCT by demonstrating OCT and autofluorescence based angiography [13–15], while others

#361933 https://doi.org/10.1364/BOE.10.003070
Journal © 2019 Received 14 Mar 2019; revised 13 May 2019; accepted 14 May 2019; published 30 May 2019

Biomedical Optics EXPRESS

used PS-OCT to highlight the presence of fibrosis [16] and collagen [17]. OCT is attracting interest for the study of lung diseases due to the ability to acquire high-resolution cross-sectional images during minimally invasive procedures [18].

In this paper, we demonstrate a multifunctional OCT platform that provides novel information on the airway wall using intensity, attenuation coefficient (AC), dynamic OCT (DOCT), and PS-OCT images with a distally scanning catheter *in vivo*, in humans. A novel automated segmentation algorithm based on the degree of polarization uniformity (DOPU) and intensity OCT images is presented. An algorithm to compensate for polarization mode dispersion (PMD) in catheter-based images improving PS-OCT imaging is described. A metric called optic axis uniformity (OAxU) is presented for highlighting fiber-like structures. The setup is demonstrated by the acquisition of images of the airways, scanning from distal to proximal, of a severe asthma patient that was scheduled for a recently-developed endoscopic severe asthma treatment called bronchial thermoplasty [19–21]. In this context, OCT, and in particular PS-OCT, seems to be a promising modality for minimally-invasive assessment of airway remodeling (*e.g.,* ASM and collagen content) and the impact of bronchial thermoplasty on the airway wall structure [22].

2. Methods

2.1 PS-OCT imaging system

Figure 1(a) shows the diagram of the imaging system, which has been described in a previous publication by Li *et al.* [17]. Light from a swept-source laser with a central wavelength of 1310 nm, bandwidth of 90 nm, and a sweep rate of 50 kHz (Axsun Inc., Billerica MA, USA) is split into a sample and reference arm of a modified Mach-Zehnder interferometer. In the sample arm, a polarization delay unit (PDU) creates two depth-encoded polarization states, orthogonal in the reference frame of the lab [23]. A circulator relays the OCT light from the PDU to the catheter and finally to the polarization diversity detection module (PDDM). The transmission reference arm configuration avoids the use of a second circulator, which is known to exhibit considerable polarization distortions [24]. A fiber-based PDDM (Finisar Corp., Sunnyvale, CA, USA) recombines the sample and reference arm and splits the orthogonal polarization components into four output leads for balanced detection, synchronized by an optical A-line trigger and a built-in k-clock.

2.2 Distally scanning OCT catheter and disinfection procedure

Figure 1(b)-(c) present a drawing of the catheter used in this study that has a distally-scanning design, similar to the one presented by Li *et al.* [17]. A single mode fiber was angle-cleaved at 8° and glued to a 0.5 mm diameter custom GRIN lens with both facets polished at 8° and a working distance of 1.5 mm (GRINTECH GmbH, Jena, Germany). An alternating current micromotor, with a diameter of 1 mm, was built in-house with double wound 90 µm diameter copper wire coils around the motor housing. A micromagnet with an axle running through its longitudinal axis is encapsulated in the motor housing. The axle is held in place by two bearings that are part of the housing, allowing the magnet to rotate freely inside the housing. The alternated current running through the wires induces a variable magnetic field that actuates the magnet by aligning its poles to the field, in turn causing the rotation of the magnet-axle construct. The doubled wound coil increased the torque on the magnet compared to our earlier implementation [17] and resulted in a more reliable rotation. A 300 µm wide reflective microprism (Edmund Optics, Barrington NJ, USA) was glued on the motor axis to reflect the light to the tissue. The microprism was glued at an angle of 48° to avoid specular backreflections from the catheter sheath, which would saturate the detectors. The axial resolution of the OCT system is 12 µm in tissue (assuming a refractive index of 1.4). The full-width-at-half-maximum spot size of the beam exiting the catheter is 13 µm.

Biomedical Optics EXPRESS

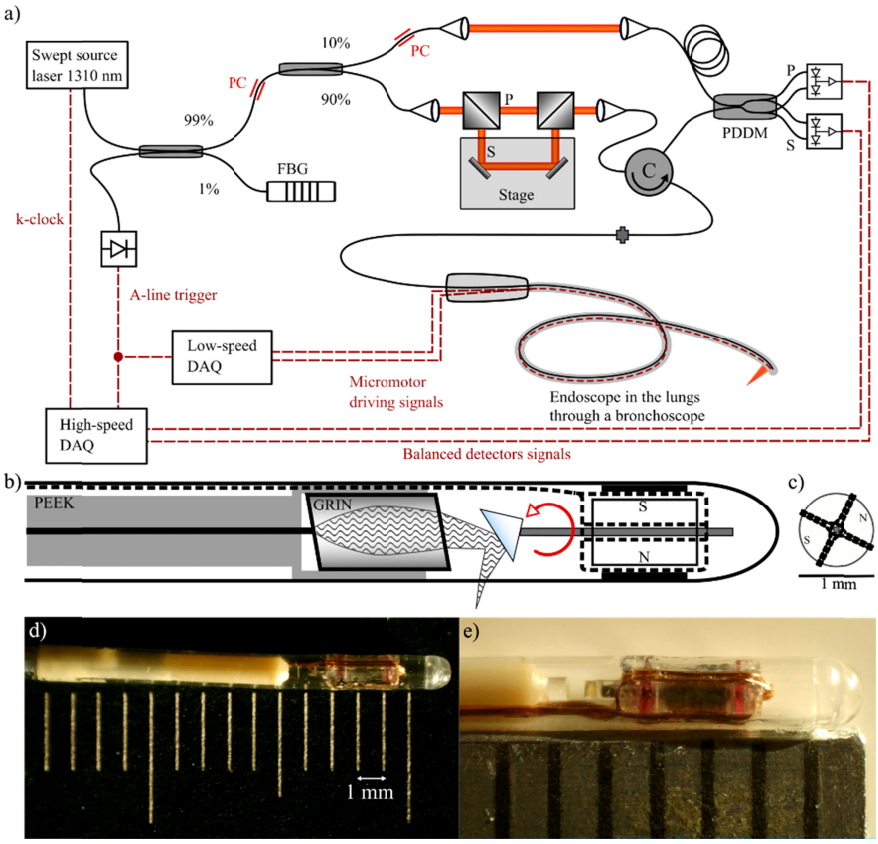

Fig. 1. Schematics of the PS-OCT imaging system, motorized OCT catheter, and custom micromotor. a) Light from a swept source laser is sampled by a fiber Bragg grating (FBG) to provide an A-line trigger. The light is split into the two arms of a Mach-Zehnder interferometer made of a reference arm with a transmission delay line and a sample arm containing a PDU that introduces a delay between P and S polarization states. A circulator (C) redirects the light to the catheter, inserted in the lungs through the working channel of a standard bronchoscope. Light from the sample arm interferes with the reference arm light in a monolithic polarization diversity detection module (PDDM), which separates the light into orthogonal polarization components (P and S) on separate balanced detectors. PCs are polarization controllers. b) A schematic of the OCT endoscope, a Peek tubing holds the single-mode fiber glued to the GRIN lens in place. The focused light is directed to the tissue by a 48° angled prism mounted on the axle of a micromotor. The rotation of the motor creates a circumferential scan that allows reconstructing an OCT B-scan. S and N represent the magnetic poles of the magnet placed at the core of the AC motor. c) cross-section of the custom micromotor. Two electrical wires are double-wound around the housing of the motor, which contains a free-to-rotate magnet with an axle held in place by two conical bearings. d) photo of the endoscope tip. e) zoom-in of the catheter tip. The copper wire double-wound on the motor is visible.

The multifunctional OCT catheter was designed and constructed to be reused several times. The hygiene requirements for pulmonology equipment are less stringent than, *e.g.*, cardiovascular catheters, and therefore disinfection of the catheters suffices for use in the lungs, compared to sterilization and single-use required for imaging arteries. The outer sheath was medical grade pebax (PEBAX 7033 SA 01 MED, Arkema, Colombes Cedex, France). Tubing made of a semi-rigid polymer (Peek) was used to protect the optical fiber inside the sheath and provide sturdiness. The catheter was filled with a clinically compatible polymer (PDMS) to fix fiber, wires and the GRIN lens in place, and to further increase the sturdiness, improving maneuverability and resistance to damages. The outer diameter of the catheter was 1.35 mm over the full length of 120 cm. A technician and hygienist of the Amsterdam

Biomedical Optics EXPRESS

University Medical Center inspected and approved the OCT catheter. After every use, the catheter was cleaned with a mixture of water and soap, wiped with an ethanol-wet gauze, and finally disinfected by a standard washing device for bronchoscopes (WD 440, Wassenburg Medical B.V., Dodewaard, The Netherlands), after being placed in a metal wire basket.

2.3 DOPU calculation

In an interferometer, only the common polarization component of reference and sample arm interfere, meaning that the measured fringes always correspond to fully polarized light. When light propagates through birefringent or scattering media, its polarization state changes. DOPU is a metric that measures the uniformity of the reflected polarization state in a portion of space. Several algorithms have been developed to calculate DOPU [25–27], with one of the most commonly used being:

$$\mathrm{DOPU}=\sqrt{\left\langle \frac{Q}{I} \right\rangle^2+\left\langle \frac{U}{I} \right\rangle^2+\left\langle \frac{V}{I} \right\rangle^2}, \tag{1}$$

where I is the intensity of the OCT backscattering at a certain location in the cross-sectional scan, and Q, U, and V its Stokes vector components obtained from the measured electric fields. The brackets indicate spatial averaging, over a kernel, sized 3x7 pixels (axially and azimuthally, corresponding to 21 µm and 2.63°), which has the effect of blurring the image. The DOPU was calculated for each depth-multiplexed polarization state independently, and the two results were averaged to obtain the DOPU used in the following steps.

In this article, DOPU was not found to carry significant diagnostic information, but it revealed to be an ideal starting point for segmenting the inner surface of the OCT catheter. Moreover, it provided a straightforward method to identify locations associated with the presence of alveoli. These structures have peculiar characteristics, namely increased backscattering at the tissue-to-air interfaces due to non-matching refractive index and weak backscattering due to the absence of scatterers within the alveoli. The DOPU in these areas is lower because of the increased contribution of noise in the low scattering areas. As demonstrated in Fig. 2(f), the areas within the orange and the cyan rectangles have similar OCT intensity. However, the corresponding DOPU image in Fig. 2(c) shows a considerably lower DOPU for the area in the orange rectangle, due to the presence of alveoli. A threshold value of DOPU of 0.7 was empirically found to isolate the alveoli from the image. This step was particularly useful to facilitate the retrieval of PMD compensation parameters, which relies on the presence of uniformly arranged fiber-like structures and the exclusion of areas subject to depolarization.

2.4 Segmentation of OCT endoscopic images

We developed a robust 3D automated algorithm to precisely segment the inner and outer edges of the endoscope sheath, the motor wires, and the surface of the airway lumen using both DOPU and intensity images. We used the segmented features to enable the PMD compensation and to improve the display of the cross sectional images.

The segmentation routine used Dijkstra's algorithm [23], which finds the shortest path linking nodes in a graph by searching the minimum value among the eight nodes neighboring a node. The graph was constructed starting from a DOPU or an intensity image, in both cases a cross section presented in polar coordinates.

Due to the blurring effect of the spatial averaging kernel, the catheter sheath structure appears as a continuous feature in DOPU images, which facilitates the detection of the inner edge of the catheter sheath. To find the inner edge of the catheter sheath in the first B-scan (n = 1), a 50 pixel thick region-of-interest (ROI) of the DOPU image is set by manual input of the upper boundary chosen by visual inspection. The ROI of the nth DOPU image is obtained

Biomedical Optics EXPRESS

by selecting a region extending 15 pixels upwards and downwards from the OCT catheter inner sheath edge from the nth-1 image.

In order to segment the inner edge of the catheter sheath, we computed the y-directional gradient of the DOPU image, where y- direction is defined as the depth direction. Secondly, we apply the shortest path search algorithm on the 50-pixel ROI of the y-directional gradient of the DOPU image where the catheter sheath inner surface is expected to be. To find the shortest path, the gradient image is transformed into a graph. The algorithm adds two extra nodes with zero cost before the first and after the last A-line of each image. These additional nodes act as a source and sink of the graph, therefore avoiding the manual endpoints selection. Once the minimum cost path is computed, the path is retrieved in the image domain, effectively segmenting the feature.

Once the inner edge of the catheter sheath is segmented, the bundled motor wires (which feed current to the motor placed at the tip of the catheter) can be localized by summing the DOPU values between the inner sheath surface (blue line in Fig. 2(c)) and the top edge of the image. The maximum value of this integral gives an approximation to the motor wire center location. The wire edges are then localized by finding the leftmost and rightmost local maxima of the DOPU integral image in a window of 300 pixels around the wire center location.

The outer edge of the catheter sheath and the upper surface of the lungs are not segmented using DOPU images because of excessive blurring. Instead, intensity images are used in the second part of the algorithm to exploit the full resolution of the images. The outer edge of the catheter sheath is found by selecting an ROI in the intensity image, which extends 30 pixels below the inner sheath surface (see Fig. 2(d)). The boundary of the outer edge of the catheter sheath is detected by using Dijkstra's algorithm on the gradient of the ROI of the intensity image. To find the tissue boundary, an ROI in the intensity images is selected, starting from one pixel below the outer surface of the catheter until the end of the imaging range. This ROI is normalized between its minimum and the maximum values. Subsequently, this ROI is denoised by applying an isotropic total variation (TV) algorithm [28], with a regularization parameter set to 50% of the ROI's standard deviation. Afterward, the denoised ROI is converted into a binary image using a threshold of 0.45. From each binary image, areas which contain zeros smaller than 50 pixels are set to ones. Finally, the lung boundaries were segmented by finding the first non-zero value from the top of the binary image for each A-line (see Fig. 2(f)). Examples of segmentation from three B-scans along the pullback are shown in Fig. 2(g)-(i), from distal to proximal locations. In Fig. 2(g) the lung tissue is almost always adherent to the outer catheter sheath, with some mucus visible next to the wires. Figure 2(h) shows a frame from the middle of the pullback, where the lumen is larger than the endoscope, and therefore the tissue appears detached. Some mucus is visible next to the wires, but the tissue is nonetheless correctly segmented. Figure 2(i) displays a B-scan from the end of the pullback where the lumen is larger than the OCT imaging range, and therefore it is not visible, apart for a faint aliased image.

Biomedical Optics EXPRESS

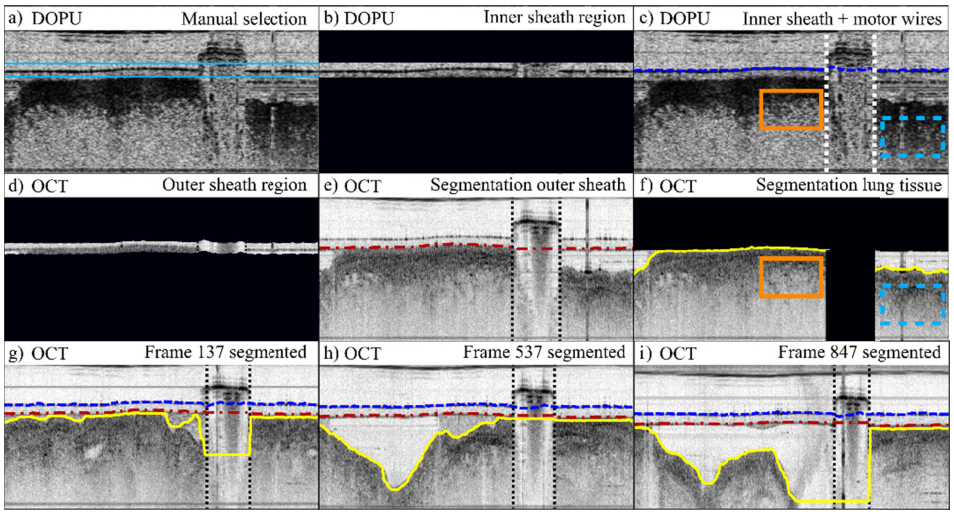

Fig. 2. Demonstration of the segmentation algorithm on OCT cross-sections shown in polar coordinates. a) Manual selection of the window for the first frame of the volume. The top boundary is chosen by visual inspection of the DOPU image of the first frame (cyan rectangle). b) The area is isolated with a binary mask, and the inner sheath surface is segmented with a graph-based shortest path algorithm. c) Segmentation of the inner sheath surface. The motor wires are detected from the integral of the DOPU image between the top edge of the image and the inner sheath surface (blue line). d) A binary mask was obtained by selecting the pixels comprised between 5 and 35 pixels below the inner sheath and applied to the intensity image. e) Segmentation of the outer sheath. f) The area above the segmented outer sheath and behind the wires is ignored and the segmentation algorithm to find the lung surface is applied. g-i) Examples of segmentation of OCT B-scans taken from different locations along the volume. The solid orange rectangle and the dashed cyan rectangle in c and f show areas associated with alveoli and submucosa, respectively.

2.5 Algorithm for PMD compensation in endoscopic PS-OCT images

The polarization distortions induced by optical fibers are detrimental to PS-OCT imaging. Some publications over the past few years have been directed to mitigate [24] or correct [29,30] PMD, which is caused by dispersion of the polarization state of the light when propagating through an optical fiber. PMD is particularly noticeable because of the broadband nature of OCT light, the considerable length of fibers involved in endoscopic imaging systems and the use of circulators, which are known for exhibiting strong PMD [24]. In this article, we use an adaptation of a PMD compensation algorithm developed for ophthalmic imaging by Braaf *et al.* [30]. Before the application of the PMD compensation algorithm, the spectra were corrected for chromatic dispersion, and a Hann window was applied. The autocorrelation of a B-scan was calculated as $\mathrm{FFT}\{S(k)^2\}$ where S(k) represents the measured interferograms. This operation was averaged over the whole cross-section, yielding two peaks, one at zero frequency and one at the frequency corresponding to the depth delay Δd between the depth encoded polarization states introduced by the PDU [31]. The depth delay Δd was determined with subpixel accuracy by determining the center of mass of the autocorrelation peak. To precisely align the electrical fields corresponding to the depth-multiplexed polarization states, a phase ramp with slope $-2\pi \cdot \Delta d$ was applied to a copy of the interferograms. Both copies of the spectra were then translated to depth domain via Fourier transformation and roll-off compensated. The top half of each matrix contained the electric fields corresponding to the depth encoded polarization states. DOPU and intensity images were produced and used to segment the inner and outer surfaces of the catheter sheath, and the wires location. The PMD compensation algorithm was carried out in the Jones formalism.

Biomedical Optics EXPRESS

The first step of the PMD compensation algorithm is finding a unique calibration region, used to determine the PMD-induced distortions caused by the imaging system and correct for them in all the B-scans of the acquired volume. Three B-scans separated in time by 100 frames were selected from the second half (more proximal part) of each C-scan, because the distal region contained more alveoli, which are depolarizing. From each of these B-scans, three consecutive 100 A-lines-wide regions were selected starting from the edge of the motor wires' shadow, yielding 9 regions. The region with the highest quality parameter (described below) was chosen as the PMD calibration region for the whole C-scan.

Analogous to Braaf *et al.* [30], the detected E-field $\mathbf{E}_{out}$ can be modeled in Jones formalism as follows:

$$\mathbf{E}_{out}(k)=\mathbf{J}_{out}(k)\mathbf{J}_{m}^{-1}\mathbf{J}_{sh}^{-1}(k)\mathbf{J}'_{S}(k)\mathbf{J}_{sh}(k)\mathbf{J}_{m}\mathbf{J}_{in}(k)\mathbf{E}_{in}(k), \tag{2}$$

with $\mathbf{E}_{in}$ the polarization state exiting the laser source, $\mathbf{J}_{in}$ the Jones-matrix for the optical path from the laser to the GRIN lens facet inside the catheter, $\mathbf{J}_{m}=\begin{bmatrix}\cos\theta & -\sin\theta\\ \sin\theta & \cos\theta\end{bmatrix}$ the Jones-matrix of the rotating mirror with angular position θ inside the catheter, $\mathbf{J}_{sh}$ the Jones-matrix for the catheter plastic sheath, $\mathbf{J}'_{S}$ the round-trip sample matrix and $\mathbf{J}_{out}$ the matrix representing the optical path from the GRIN lens facet to the detectors.

As introduced in Ref [30], the PMD-compensation is performed in two steps. The algorithm is summarized in Fig. 3. The first step aims at the elimination of the matrix $\mathbf{J}_{out}(k)$. The four complex depth-domain signals (two orthogonal polarization detectors and two depth-multiplexed polarization states) of each region are translated back to the wavenumber domain. Each spectrum is binned into 15 overlapping Gaussian-shaped bins and each Fourier-transformed to depth domain. The electric fields corresponding to the previously segmented catheter sheath outer surface were selected for each bin, yielding $\mathbf{E}_{surf}(\text{bin})$. By interpolating the 15 $\mathbf{E}_{surf}(\text{bin})$ over the whole wavenumber-spectrum, $\mathbf{E}_{surf}(k)$ was obtained, which is modeled as:

$$\mathbf{E}_{surf}(k)=\mathbf{J}_{out}(k)\mathbf{J}_{m}^{-1}\mathbf{J}_{sh}^{-1}(k)\begin{bmatrix}1 & 0\\ 0 & -1\end{bmatrix}\mathbf{J}_{sh}(k)\mathbf{J}_{m}\mathbf{J}_{in}(k)\mathbf{E}_{in}(k). \tag{3}$$

Here, the matrix [1,0;0,-1] represents the surface reflection at the catheter outer wall (or as in Ref [30]. the sample surface reflection). The influence of the mirror rotation is causing the surface state to change periodically and induces phase wrapping of the surface state at specific locations in the B-scan. Since the surface state was calculated over three adjacent segments of 100 A-lines, the surface state $\mathbf{E}_{surf}(k)$ from a segment which did not show any phase wrapping was chosen. The inverse of the obtained $\mathbf{E}_{surf}(k)$ is multiplied to the field measured from the sample to eliminate the matrix $\mathbf{J}_{out}(k)$:

$$\mathbf{E}_{surf}^{-1}(k)\mathbf{E}_{out}(k)=\mathbf{E}_{in}^{-1}(k)\mathbf{J}_{in}^{-1}(k)\mathbf{J}_{m}^{-1}\mathbf{J}_{sh}^{-1}(k)\mathbf{J}_{S}(k)\mathbf{J}_{sh}(k)\mathbf{J}_{m}\mathbf{J}_{in}(k)\mathbf{E}_{in}(k), \tag{4}$$

where the reflection matrix and the matrix $\mathbf{J}'_{S}(k)$ were included in the matrix $\mathbf{J}_{S}(k)$. It is noteworthy that the matrices surrounding $\mathbf{J}_{s}$ are canceling only for the same location on the catheter sheath, which was approximately achieved by limiting the analysis to a segment of 100 adjacent A-lines (corresponding to 37.5° of prism rotation). The left side of Eq. (4) becomes the identity matrix when the field $\mathbf{E}_{out}(k)$ corresponds to the surface of the sample, which was required by the PMD compensation algorithm [30].

Biomedical Optics EXPRESS

In the second step of the PMD compensation, an additional correction matrix $\mathbf{Q}_{in}(k)$ is derived through eigendecomposition [30] and applied together with $\mathbf{E}_{surf}(k)$ to the spectra of an evaluation B-scan according to the equation in Fig. 3. Modeling the optical fibers as pure retarders (therefore assuming negligible diattenuation), their Jones matrices are unitary and belong to the SU(2) group. Therefore, the matrix on the left side of the Eq. (4) and the inner matrix $\mathbf{J}_S$ of the right side of the same equation share the same eigenvalues. Eigendecomposing the left side of the equation allows reconstructing the birefringence properties of $\mathbf{J}_S$.

The local phase retardation image obtained through the algorithm explained in section 2.6 was then calculated, and only for pixels with a DOPU higher than 0.7 the local phase retardation values were plotted in a histogram. A quality parameter QP was calculated as the ratio between the height and full-width-at-half-maximum (FWHM) of the histogram peak. In the experimental data, most tissue pixels represent non-birefringent tissue. Therefore the FWHM is mostly dominated by the noise floor of the local birefringence in tissue. Consequently, QP increases when the retardation noise floor is reduced, increasing the SNR of the birefringence images, which is the objective of the algorithm. QP was measured for each PMD compensation region, and the region that showed the highest QP was chosen to correct the PMD in the whole C-scan.

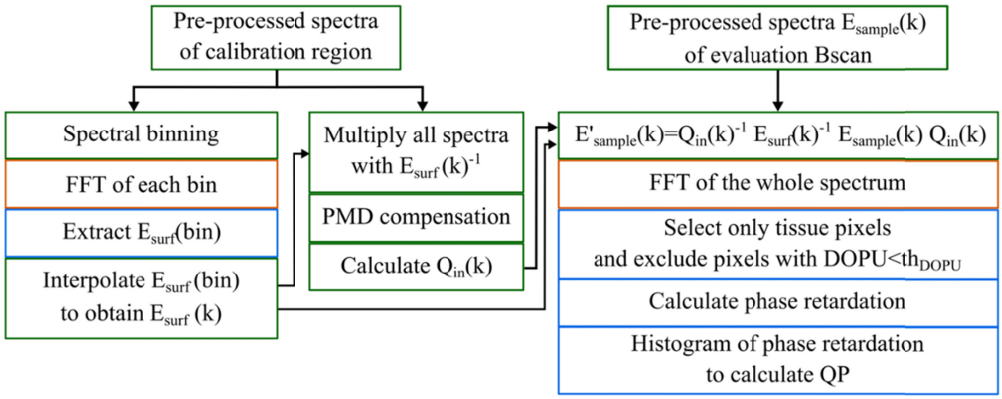

Fig. 3. Schematic of the PMD compensation algorithm. The boxes in green represent operations in the wavenumber domain, while the boxes in blue operations in depth-domain. The orange boxes represent Fast Fourier Transforms (FFT).

2.6 Stokes formalism-based birefringence extraction

While the PMD compensation algorithm described in paragraph 2.5 is based on Jones formalism, the birefringence properties have been extracted using Mueller-Stokes formalism. Villiger *et al.* [32] pointed out that Mueller matrices and Stokes vectors allow easier spatial averaging because they are real quantities. Despite being able to obtain equivalent results, Jones-based algorithms require proper management of the global phase for spatially averaging the complex Jones vectors and matrices. Instead of converting the measured Jones vectors into Stokes vectors, we combined the four measured complex components in a 2x2 matrix and converted it into a Mueller measurement matrix, also called Jones-Mueller matrix. First, the polarization properties of a segment of tissue are isolated from the ones of the rest of the tissue and the PS-OCT system by multiplying a Jones-Mueller matrix $\mathbf{JM}$ from location $z+\Delta z$ to the inverse of the Jones-Mueller matrix of location z, yielding the matrix $\mathbf{M}$:

$$\mathbf{M} = \mathbf{JM}(z+\Delta z)\mathbf{JM}(z)^{-1}. \tag{5}$$

Biomedical Optics EXPRESS

The phase retardation is then extracted from the differential Mueller matrix **m**. Assuming that the sample is homogeneous over a small depth Δz, the differential Mueller matrix can be calculated as the matrix logarithm of the Mueller matrix. To speed up the calculations, the matrix logarithm was computed using an approximation [32]:

$$\mathbf{m} = \mathrm{logm}(\mathbf{M}) \approx \frac{\mathbf{M}}{\sqrt[4]{\det(\mathbf{M})}} - \mathbf{I}, \tag{6}$$

where **I** is the 4x4 identity matrix. Azzam [33] showed that the birefringence around the Q, U, and V axes is represented by a subset of the off-diagonal elements of the differential Mueller matrix in a first-order approximation:

$$\Gamma = \begin{bmatrix} \eta \\ \nu \\ \mu \end{bmatrix} = \frac{1}{2}\begin{bmatrix} m_{34} - m_{43} \\ m_{24} - m_{42} \\ m_{23} - m_{32} \end{bmatrix}, \tag{7}$$

where the first and second number indices indicate row and columns of the matrix **m**. The major advantage of this algorithm is that its output Γ is a 3D vector whose direction represents the orientation of the sample optic axis in Poincare space while its magnitude $\gamma = \sqrt{\eta^2 + \nu^2 + \mu^2}$ corresponds to the amount of phase retardation induced by the sample. The local retardation was measured over a distance of 55.8 μm in tissue (assuming a refractive index of 1.4). The local retardation (birefringence) images are displayed in the range [0 1] radians to maximize the contrast, corresponding to [0 0.51]°/μm in birefringence units according to: $\frac{\gamma \cdot 180°}{2\pi \cdot \Delta z}$, or [0 2.5·10–3] according to $\Delta n = n\frac{\gamma \cdot \lambda_0}{4\pi \cdot \Delta z}$, where n is the medium refractive index and λ_0 the central wavelength of the OCT beam.

2.7 Quantifying optic axis uniformity

The optic axis (OA) orientation of a birefringence sample can be determined with PS-OCT. The round-trip nature of the measurement restricts the measurement to the QU plane of the Poincare sphere. However, due to the birefringence of the fibers, the measured sample optic axes appear on a tilted plane on the Poincare sphere. Rotating this plane back on the QU plane introduces a π ambiguity because two equivalent rotations bring the optic axes plane to the QU-plane, implying that generally only the relative OA orientation is shown [34]. Tissue that is arranged in a fiber-like structure, *e.g.,* collagen and muscle, typically exhibits form birefringence. If the fibers are oriented in the same direction, the OA will show consistent orientation throughout the sample. In this paper, we used a simple metric that evaluates the uniformity of the sample OA [35], previously described in a similar form by Yamanari *et al.* [36]. The OA orientation was determined from the direction of the real three-dimensional vector Γ extracted as in 2.6. By evaluating the spatial uniformity of the normalized vectors over a small portion of the sample, the optic axis uniformity (OAxU) was extracted as:

$$\mathrm{OAxU} = \sqrt{\left\langle \frac{\eta}{\gamma} \right\rangle^2 + \left\langle \frac{\nu}{\gamma} \right\rangle^2 + \left\langle \frac{\mu}{\gamma} \right\rangle^2}, \tag{8}$$

where η, ν and μ are the components of the vector Γ along the Poincare space axes and γ is the length of the vector Γ, while the angular brackets represent spatial averaging over a small volume. Using this definition restricts the values of OAxU between 0 and 1. Determining the OA orientation is particularly useful for highlighting areas of a sample with uniformly arranged fiber-like structures, as pointed out by Adams *et al.* [11], so we suggest that OAxU

Biomedical Optics EXPRESS

could be an intuitive metric to achieve this goal. Moreover, catheter-based PS-OCT systems require to account for the varying polarization state impinging on the tissue throughout the catheter rotation, which complicates retrieval of the OA orientation [12,37,38]. By choosing an appropriately sized averaging kernel, a constant sampling polarization state can be assumed, circumventing the management of the rotating surface polarization state. In this case, OAxU was calculated over a two-dimensional spatial kernel sized 4x18pixels, corresponding to 26 μm in depth and 7° along the azimuthal direction.

2.8 DOCT based on adjacent A-line phase difference

DOCT is a popular method to highlight the presence of blood flow in OCT images. DOCT measures the phase difference between interferograms acquired from the same location at different points in time. Scatterers that have moved in that period create a phase shift of the reflected field from that location. This method requires high phase stability to measure flow in small blood vessels. In the case of endoscopic OCT, the preceding pivoting point and non-uniform rotational distortions (NURD) introduce artificial axial and lateral motion, in turn leading to phase jitter. These effects are strong in proximal scanning catheters, but there are nonetheless examples of DOCT with such devices [13,39]. To this end, distally scanning catheters are more suitable, and examples of angiographic images produced with micromotor-based catheters have been shown [40,41].

To extract DOCT images, we corrected for the phase jitter in the axial direction of the images. In our algorithm, the first step was combining the four measured fields into one by adding the complex fields [42]. In the second step, each A-line $\mathbf{E}_{z,\rho}$ was multiplied with the complex conjugate $\mathbf{E}^{*}_{z,\rho-1}$ of its adjacent A-line, where ρ denotes the angular location throughout the motor rotation. After applying a binary mask to exclude low-SNR regions, the complex signals along the z-direction were coherently added for each angular location. In formula:

$$\theta_{\rho} = \arg\left(\sum\nolimits_{z}\left(\mathbf{E}_{z,\rho}\cdot\mathbf{E}^{*}_{z,\rho-1}\right)\right). \tag{9}$$

This method is equivalent to creating a weighted average of the phase because vectors (phasors) with greater magnitude contribute more to the sum. The phase component θ_{ρ} of the phasor sum was subtracted from each axial location of the complex phase-difference signal $\mathbf{E}_{z,\rho}\cdot\mathbf{E}^{*}_{z,\rho-1}$, compensating for bulk motion [43,44]. Spatial averaging of the resulting fields was obtained by convoluting the complex fields with a Gaussian kernel sized twice the optical resolution in both dimensions. In formula:

$$\Delta\varphi_{z,\rho} = \arg\left(\text{kernel}\otimes\left(\mathbf{E}_{z,\rho}\cdot\mathbf{E}^{*}_{z,\rho-1}\cdot e^{-i\theta_{\rho}}\right)\right). \tag{10}$$

This process guarantees a low noise floor in the phase-difference image. Finally, the square of the phase component $\Delta\varphi_{z,\rho}$ of the signal was Gaussian filtered with a kernel size of twice the resolution. A threshold of 0.63 rad was chosen to display the phase difference data as a binary image overlapped with the PS-OCT images.

2.9 AC calculation

Images based on the depth-resolved AC of the tissue were produced to improve the interpretation of images. Since the optical energy is not fully dissipated in the tissue and we did not incorporate correction for beam shape and focus position [45–47], the AC images were used for qualitative evaluation only. The calculation was based on the algorithm developed by Vermeer *et al.* [48], which uses chromatic dispersion corrected and roll-off compensated intensity OCT images in linear scale. According to Eq. (18) in Ref [48], the AC

Biomedical Optics EXPRESS

μ_i of each depth location i is estimated by dividing the intensity I_i of each depth pixel I by the sum of the intensities of the pixels underneath:

$$\mu_i \simeq \frac{I_i}{2\Delta z \sum_{i+1}^{\infty} I_i} \tag{11}$$

where Δz is the distance between two consecutive depth pixels and the factor 2 accounts for the double pass of the light into the tissue. Finally, the AC image was produced by taking the base-10 logarithm of the data and displaying them in an inverted greyscale ranging from $10^{-1.8}$ to $10^{2.7}$ mm^{-1} (45 dB range).

2.10 Imaging protocol patient criteria

This severe asthma patient participated in the TASMA trial (trial.gov number NCT02225392). The Ethics committee of the hospital approved the protocol. During bronchoscopy, OCT imaging was performed in two basal segments of the right lower lobe. In short, after advancing the tip of a therapeutic bronchoscope until the segmental airways, the OCT-catheter was inserted through the working channel with an inner diameter of 2.8 mm (Olympus, Tokyo, Japan). After that, the OCT catheter was advanced to the pleura and subsequently retracted by a manual slow-pull technique for image acquisition. The slow pullback was repeated once over the same length of approximately 10 cm to create two image data sets of the same area.

2.11 Examples of histology of the human airway wall

Human airway histological slides were obtained from patients that were scheduled for lobectomy because of non-small cell lung cancer (Ethics approved; NL51605.018.14). *Ex-vivo* non-diseased airways were dissected, sectioned and analyzed. Human airway histology sections are shown here as a comparison for the (PS-)OCT images presented in the next section. 5 µm-thick histological sections were stained with two different stains: hematoxylin and eosin (H&E) and ASM-specific desmin. Figure 4(a)-(b) show an example of each type of staining. The main histological features of human airways are distinguishable in H&E staining (Fig. 4(a)), such as epithelium (cyan arrow), basement membrane (grey arrow), lamina propria (pink arrow), and smooth muscle (blue arrow). The red arrow in Fig. 4(a) indicates a piece of cartilage. Desmin staining locates ASM, which appears as brown-colored parts of Fig. 4(b). The main histological features can also be identified in OCT cross-sections acquired *in vivo* from a human bronchiole, as shown by Fig. 4(c)-(d), which present a traditional OCT intensity image and the AC image of the same frame.

Biomedical Optics EXPRESS

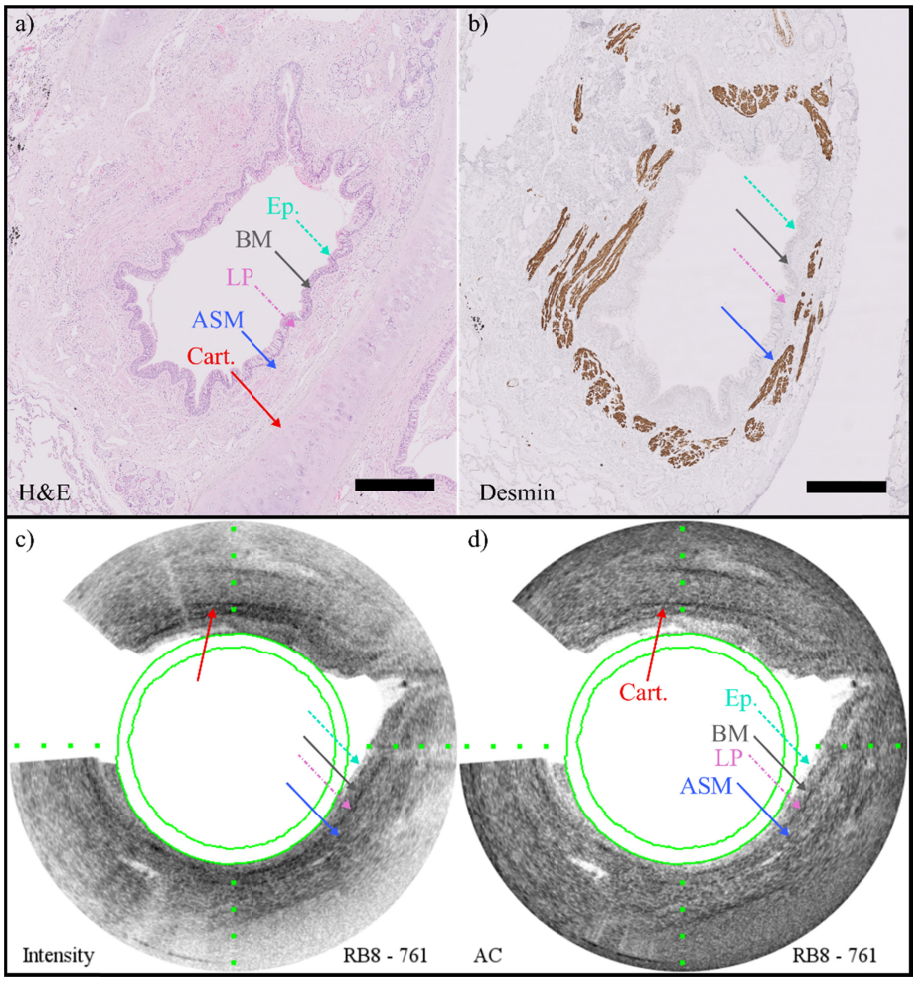

Fig. 4. An example of histology of a human bronchus compared with cross sections acquired *in vivo* with our OCT catheter. a) H&E staining of an airway cross section. b) Desmin staining of an airway cross section. c) OCT intensity image acquired *in vivo* from a bronchiole of a severe asthma patient (not the same patient from which the histological slides were obtained). d) AC image of the same cross-section. In all images, the arrows indicate the main histological features of the airway: epithelium (Ep.), basement membrane (BM), lamina propria (LP), airway smooth muscle (ASM), and cartilage (Cart.). The scale bar in the histological images is 500 µm. The distance between the dotted green markers in the OCT images is 200 µm in tissue.

3. Results

We acquired two pullbacks from two different segments of the right segmental bronchus (RB) of a human lung, *in vivo*. First, traditional OCT images are compared to AC images to show the potential of AC for artifacts-corrected structural imaging. Then, phase retardation and OAxU images are compared to intensity and AC images to show the added benefit of PS-OCT imaging for highlighting fiber-like structures in the lungs. The DOCT signal is added to the PS-OCT to help identifying blood vessels. The images produced with the OCT catheter are shown in cartesian coordinates to represent the actual geometry of the airway wall.

3.1 Comparison of OCT intensity images and AC images

The AC images calculated according to the method explained in section 2.9 provide a different representation of the same information in typical OCT intensity images. In this

Biomedical Optics EXPRESS

section, OCT intensity images are compared with AC images to show improved architectural contrast displayed by AC images. Both types of images are shown on a logarithmic scale, with a −55 dB dynamic range for the OCT intensity and $[10^{-1.8}\ 10^{2.7}]$ mm^{-1} for the AC images (dynamic range of 45 dB). The AC units are not quantitative since the corrections of the catheter optical properties were not included. In Fig. 5, two frames from one of the pullbacks in the patient are shown. The OCT intensity images suffer from artifacts caused by a non-uniform spatial distribution of tissue types with different optical properties. The AC image shows superior contrast for deeper structures. A piece of cartilage, indicated by the red arrows in Fig. 5(a),(b), is more clearly visible in the AC images because of the corrected shadowing artifacts and improved contrast between tissue layers by the display of the local scattering properties. The generally improved contrast in AC images can be appreciated from frame 197 to frame 259 of Visualization 1.

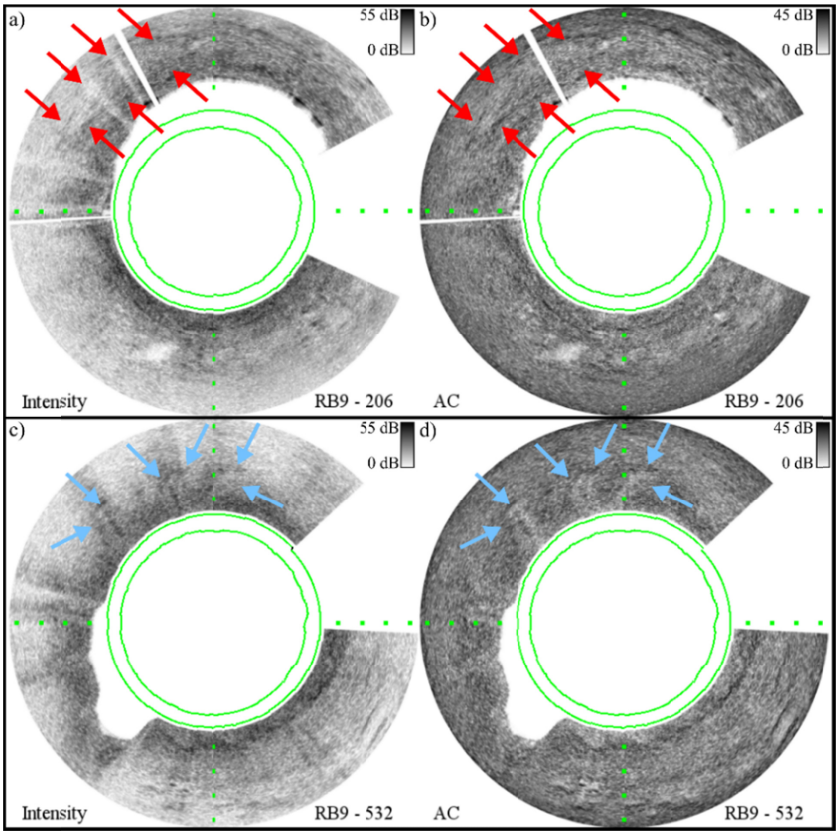

Fig. 5. Comparison of OCT intensity images and AC images extracted with the depth-resolved AC method. In all figures, the green circles represent the inner and outer edge of the plastic catheter sheath. The white area on the right half of the images masks the area of tissue not optically accessible due to the presence of the copper wires feeding current to the motor, obtained from the segmentation algorithm. The thin white lines are A-lines excluded due to saturation of the photodetectors. a,c) OCT intensity image of a frame along the *in vivo* pullback in a patient with chronic asthma. b,d) AC image of the same cross-section. The red arrows in a) indicate artifacts that are partially obscuring a piece of cartilages, corrected by the AC calculation in b). The light blue arrows in c) and d) point at areas where epithelial folds are present but only visible in the AC images. The greyscale is [0 −55] dB for the OCT intensity images in a) and c), and $[10^{-1.8}\ 10^{2.7}]$ mm^{-1} for the AC images in b) and d). The distance between the dotted green markers is 200 µm in tissue.

In Fig. 5(c), what seems to be tissue with low attenuation causes some parts of the OCT image to have a high intensity, as indicated by the light blue arrows. Since AC images display

Biomedical Optics EXPRESS

local attenuation or scattering density, these artifacts disappear, as indicated by the light blue arrows in Fig. 5(d). The tissue in the superficial areas indicated by the same arrows resemble folded epithelial layers, typical of relaxed bronchioles, as shown in histological slides such as the ones of Fig. 4. It is noteworthy that these structures are almost indistinguishable in the intensity OCT image (Fig. 5(c)). These examples of folded epithelial layers are apparent in Visualization 1 from frame 490 to frame 560 in the top half of the image.

3.2 PS-OCT and DOCT in vivo imaging of pulmonary airways

The retrieved PS-OCT show several features that are not visible in the OCT or AC images. Some of these features are particularly striking in the OAxU images, which highlight the presence of fibers oriented consistently in a small portion of tissue. Histological cross-sectional images of airway walls reveal the presence of several types of tissue with fiber-like properties, such as ASM and connective tissue layering the cartilage (see Fig. 4). ASM is expected to show high OAxU because of its consistently-oriented fibers. Cartilage is surrounded by a layer of connective tissue, the perichondrium, which suggests that its presence will appear in retardation images as a ring of high birefringence.

In this section, we present several exemplary frames from the OCT volumes, which are available as supplementary material [Visualization 1 and Visualization 2].

Figure 6 and Fig. 7 show two frames of the volume obtained *in vivo* from location RB8. The blue arrows in Fig. 6(c),(d) indicate a layer of tissue with strong birefringence and high OA uniformity, located about 200 µm from the lumen surface. The layer probably corresponds to ASM. The blue arrows in Fig. 6(a),(b) point at the same area in the intensity and AC images, but delineating the same structures is significantly more difficult. However, the ASM layer seems to show a reduced scattering coefficient and to be surrounded by two thin highly scattering layers, visible in Fig. 6(b). The alveoli at the black arrow location in Fig. 6(a),(b) appear as low-scattering areas. The orange arrows point at large blood vessels, clearly visible from the strong DOCT signal, which appears in red in Fig. 6(c),(d).

Biomedical Optics EXPRESS

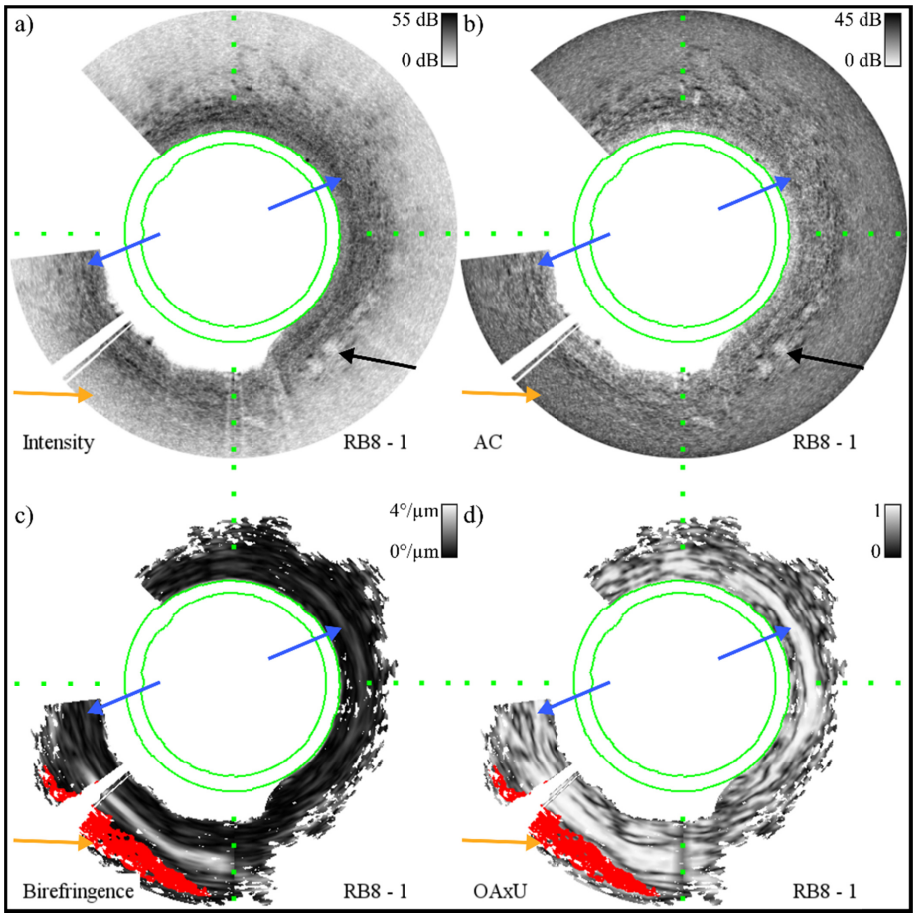

Fig. 6. Example of a cross section from a distal location along the *in vivo* pullback in RB8. a) Intensity OCT B-scan. b) Corresponding AC image. c) Birefringence-induced local phase retardation image of the same frame. In red the DOCT signal. d) OAxU of the same frame. The black arrows indicate alveoli. The blue arrows point to a superficial birefringent layer, probably associated with the presence of ASM, which is visible in the birefringence images, and more prominently visible in the OAxU images. In all images, the orange arrows indicate a blood vessel. The green circles represent the edges of the plastic catheter sheath, as found by the segmentation algorithm. The white area on the top left side of the images masks the area of tissue not optically accessible due to the presence of the copper wires feeding current to the motor, while the thin white lines are A-lines excluded due to saturation of the photodetectors. The intensity images have a greyscale dynamic range of 55 dB, the AC images are shown on a logarithmic scale of $[10^{-1.8}\ 10^{2.7}]$ mm^{-1}, the birefringence images are shown between [0 4.0]°/µm, the greyscale range of OAxU images is [0 1], while the DOCT signal is shown as a binary image above a threshold of 0.63 rad. The distance between the dotted green markers is 200 µm in tissue.

Figure 7 presents a proximal frame along the pullback in RB8, the same presented in Fig. 4. The red arrows in Fig. 7 indicate two pieces of cartilage. These structures are lined by a layer with high birefringence and OA uniformity (the perichondrium), as clearly visible in Fig. 7(c),(d). This layer is also more scattering than the content of the cartilage, as shown in Fig. 7(b). The blue arrows indicate a layer which probably represents ASM, while the orange ones a blood vessel.

Biomedical Optics EXPRESS

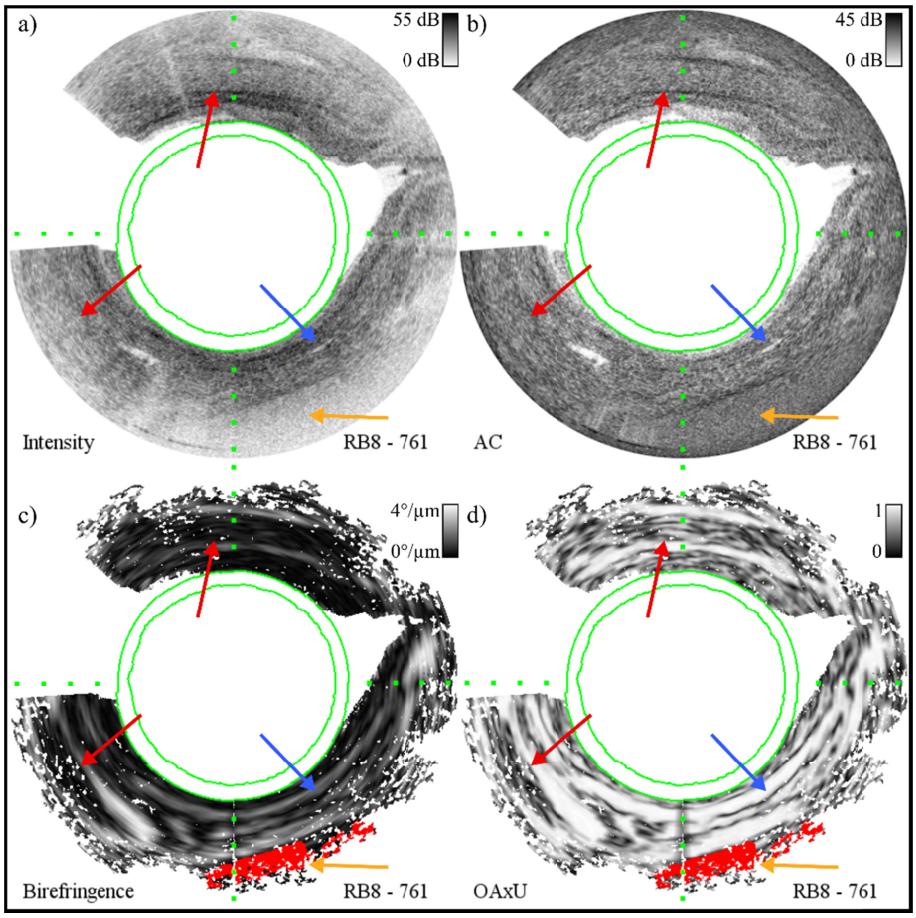

Fig. 7. Example of a cross section from a proximal location along the *in vivo* pullback in RB8. a) Intensity OCT B-scan. b) Corresponding AC image. c) Birefringence-induced phase retardation image of the same frame. In red the DOCT signal. d) OAxU of the same frame. The red arrows point at two large pieces of cartilage, with their perichondrium appearing as a ring-like structure. The blue arrows point to a birefringent layer, probably associated with the presence of ASM, which is visible in the birefringence images, and more prominently visible in the OAxU images. In all images, the orange arrows indicate blood vessels, while the green circles represent the edges of the plastic catheter sheath, as found by the segmentation algorithm. The white area on the top left side of the images masks the area of tissue not optically accessible due to the presence of the copper wires feeding current to the motor. The intensity images have a greyscale dynamic range of 55 dB, the AC images are shown on a logarithmic scale of $[10^{-1.8}\ 10^{2.7}]$ mm^{-1}, the birefringence images are shown between [0 4.0]°/µm, the greyscale range of OAxU images is [0 1], while the DOCT signal is shown as a binary image above a threshold of 0.63 rad. The distance between the dotted green markers is 200 µm in tissue.

Figure 8 and Fig. 9 show two frames of a pullback from a bronchiole located in RB9. Once again, the PS-OCT images reveal several layers that are not easily discernible in the intensity OCT and AC images. For example, the blue arrows indicate a contiguous birefringent layer, associated with ASM, extending for a large part of the airway wall. The ASM layer appears surrounded by a highly scattering thin lining in the AC image (Fig. 8(b)). The dashed green arrows point at a weakly birefringent superficial layer, possibly associated with the presence of elastin in the mucosa. The red arrows indicate a piece of cartilage.

Biomedical Optics EXPRESS

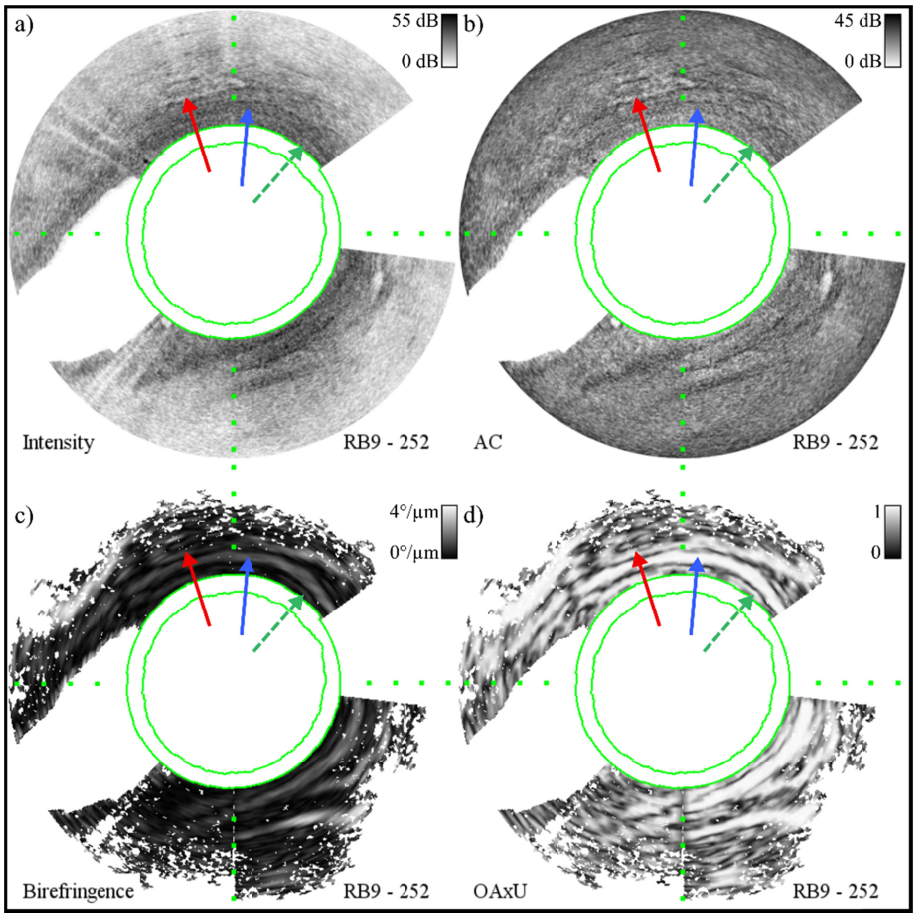

Fig. 8. Example of a cross section from a distal location along the *in vivo* pullback in RB9. a) Intensity OCT B-scan. b) Corresponding AC image. c) Birefringence-induced phase retardation image of the same frame. In red the DOCT signal. d) OAxU of the same frame. The solid red arrows point at a piece of cartilage. The blue arrows indicate ASM, while the dashed green arrows a superficial birefringent structure of unknown origin. In this frame, no blood flow was detected by our phase-resolved algorithm. In all images, the green circles represent the edges of the plastic catheter sheath, as found by the segmentation algorithm. The white area on the right side of the images masks the area of tissue not optically accessible due to the presence of the copper wires feeding current to the motor. The intensity images have a greyscale dynamic range of 55 dB, the AC images are shown on a logarithmic scale of $[10^{-1.8}\ 10^{2.7}]$ mm^{-1}, the birefringence images are shown between [0 4]°/µm, the greyscale of OAxU images is [0 1], while the DOCT signal is shown as a binary image above a threshold of 0.63 rad. The distance between the dotted green markers is 200 µm in tissue.

Two pieces of cartilage, whose perichondrium show the characteristic ring-like structure in the PS-OCT images, are visible in Fig. 9, indicated by the red arrows. The OAxU image once again helps in highlighting an extended layer with high OA uniformity and birefringence, associated with ASM and indicated by the blue arrows. The dashed green arrows point at a weakly birefringent layer in the mucosa. A blood vessel is visible in the top left quadrant of the images.

Biomedical Optics EXPRESS

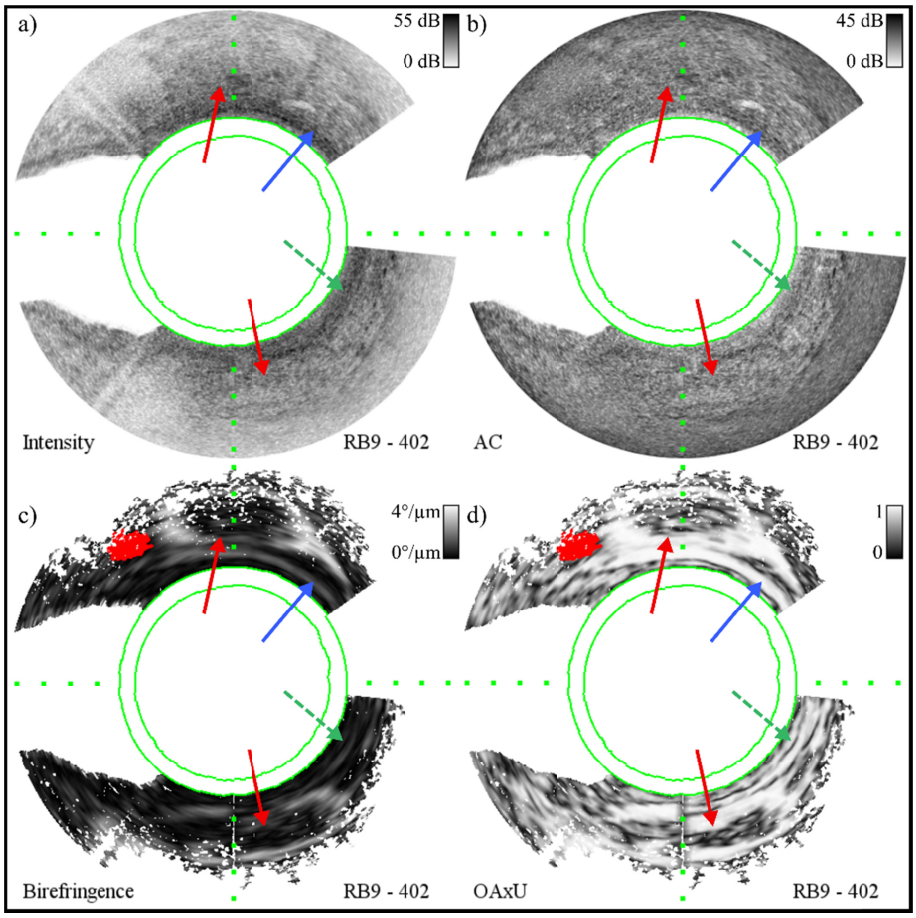

Fig. 9. Example of a cross section from a proximal location along the *in vivo* pullback in RB9. a) Intensity OCT B-scan. b) Corresponding AC image. c) Birefringence-induced phase retardation image of the same frame. In red the DOCT signal. d) OAxU of the same frame. The red arrows indicate two pieces of cartilage, while the blue arrows ASM. The dashed green lines highlight the presence of a shallow birefringent layer of uncertain origin. A blood vessel is visible in the top left quadrant of the image. In all images, the green circles represent the edges of the plastic catheter sheath, as found by the segmentation algorithm. The white area on the right side of the images masks the area of tissue not optically accessible due to the presence of the copper wires feeding current to the motor. The intensity images have a greyscale dynamic range of 55 dB, the AC images are shown on a logarithmic scale of $[10^{-1.8}\ 10^{2.7}]$ mm^{-1}, the birefringence images are shown between [0 4]°/µm, the greyscale of OAxU images is [0 1], while the DOCT signal is shown as a binary image above a threshold of 0.63 rad. The distance between the dotted green markers is 200 µm in tissue.

4. Discussion

In this article, a reusable motorized OCT catheter was used for the first time to acquire *in vivo* data from the peripheral bronchi of a human lung. Two volumes were acquired from a severe asthma patient that underwent a baseline bronchoscopy before bronchial thermoplasty. Several types of OCT contrast were extracted from the data, namely: OCT intensity images, AC images, DOCT, and PS-OCT, showing both phase birefringence and OAxU images.

For the first time, AC images were used in airway lumens to correct for artifacts in the traditional OCT images arising from the non-uniform distribution of scatterers across the lumen. Although initially difficult to interpret due to their novelty, AC images provide superior contrast of the lung airways compared to intensity images. In particular, epithelial

folds are often only visible in the AC images. Structures in deep locations are more prominent in AC images, which show alveoli and cartilage with higher contrast compared to traditional OCT images, suggesting that AC images might be a better method to show tissue structure in OCT images of the airways. Moreover, corrected AC images might offer an additional foundation for discriminating different types of tissue based on their attenuation properties.

The PS-OCT images highlight the presence of several layers of tissue in the airway wall, which are not easily distinguishable in the structural OCT images. A metric that highlights the presence of uniformly oriented birefringent tissue in a small portion of tissue, OAxU, was used for the first time to delineate layers of ASM and connective tissue in the airway lumen, which can be analyzed in more detail in the birefringence images. As already pointed by Adams *et al.* [11], identifying the OA orientations provides a more robust way of highlighting the presence of ASM, compared to birefringence images. OAxU simplifies this goal by circumventing the need of complex algorithms that compensate for the rotation of the motor (or of the catheter in case of proximal scanning setups) to find the absolute OA orientation, which was the objective of three recent publications [12,37,38]. Since tissue remodeling affects the ASM in the airway wall, OAxU might be a straightforward method to assess the effect of bronchial thermoplasty. Nevertheless, the OAxU images require further investigation to improve the interpretation of this feature-rich modality. Local phase retardation images add information by providing a measurement related to the density of the fiber-like structures in the image.

The DOCT signal reveals large blood vessels close to the airway wall. The NURD of the OCT catheter hampers the detection sensitivity of slow blood flow with DOCT. Good quality angiography of the human airways has been shown exploiting blood autofluorescence [15,49]. If angiography is hypothesized to have diagnostic value for asthma, fluorescence detection could be integrated into the OCT catheter using double-clad fibers as shown in [50].

Precise segmentation of the inner and outer surfaces of the catheter is crucial for performing the PMD and axial bulk motion compensation algorithms presented in this work, therefore improving the quality and reliability of the PS-OCT and DOCT images. Moreover, the segmentation allows removing parts of the image that could be distracting, such as the area within the catheter sheath and the area of tissue obstructed by the wires.

In conclusion, the setup and the algorithms demonstrated in this article further support the suggestion that multifunctional OCT, and in particular PS-OCT, is an adequate tool in terms of specificity, resolution, and field-of-view for the study of tissue remodeling in human airways. PS-OCT imaging might qualify as a high-resolution real-time imaging technique to assess airway wall tissue remodeling in chronic airways diseases, including asthma.

Contributions

FF built the PS-OCT system and designed the OCT catheter. FF, PIB, AWG and JTA acquired the data. DvI designed and built the custom micromotor and assembled the catheter. VD developed and implemented the segmentation algorithm and wrote the AC code. JW, MGOG, and FF adapted the PMD compensation algorithm. JW, FF, MGOG, and JFdB devised the OAxU and Mueller based algorithms. JAMD performed the first *in vivo* animal and human measurements to assess the catheter safety. JFdB supervised the project and acquired the funding. FF wrote the manuscript with contributions from JW, VD, MGOG, AWMG, PIB, and JFdB. All authors revised the manuscript.

Funding

Netherlands Organization for Scientific Research (NWO) (918.10.628); LaserLaB-Europe (grant # EC-GA 654148); Dutch Lung Foundation (5.2.13.064); ZonMw (90713477); Boston Scientific.

Biomedical Optics EXPRESS

Acknowledgments

The authors would like to thank the technicians of the VU Amsterdam: Jelmer J.A. Weda for assistance with the development of the OCT catheter and during the imaging sessions, Wesley Delmeer, Han Voet, and Rob J. Limburg for developing the drivers of the catheter motor, and Joost C. Rosier for coordinating the technical efforts. We would like to thank Margherita Vaselli for helping during the imaging sessions. We would like to thank UMC hygienists Leo Walgering and Harry van Ousoren for reviewing the OCT catheter, giving valuable feedback on the design and devising the disinfection procedure.

Disclosures

The authors declare that there are no conflicts of interest related to this article.

References

1. E. A. Swanson and J. G. Fujimoto, "The ecosystem that powered the translation of OCT from fundamental research to clinical and commercial impact [Invited]," Biomed. Opt. Express **8**(3), 1638–1664 (2017).
2. M. Tsuboi, A. Hayashi, N. Ikeda, H. Honda, Y. Kato, S. Ichinose, and H. Kato, "Optical coherence tomography in the diagnosis of bronchial lesions," Lung Cancer **49**(3), 387–394 (2005).
3. S. Lam, B. Standish, C. Baldwin, A. McWilliams, J. leRiche, A. Gazdar, A. I. Vitkin, V. Yang, N. Ikeda, and C. MacAulay, "In vivo optical coherence tomography imaging of preinvasive bronchial lesions," Clin. Cancer Res. **14**(7), 2006–2011 (2008).
4. R. G. Michel, G. T. Kinasewitz, K.-M. Fung, and J. I. Keddissi, "Optical Coherence Tomography as an Adjunct to Flexible Bronchoscopy in the Diagnosis of Lung Cancer," Chest **138**(4), 984–988 (2010).
5. L. P. Hariri, M. Mino-Kenudson, M. Lanuti, A. J. Miller, E. J. Mark, and M. J. Suter, "Diagnosing Lung Carcinomas with Optical Coherence Tomography," Ann. Am. Thorac. Soc. **12**(2), 193–201 (2015).
6. A. D. Lucey, A. J. King, G. A. Tetlow, J. Wang, J. J. Armstrong, M. S. Leigh, A. Paduch, J. H. Walsh, D. D. Sampson, P. R. Eastwood, and D. R. Hillman, "Measurement, reconstruction, and flow-field computation of the human pharynx with application to sleep apnea," IEEE Trans. Biomed. Eng. **57**(10), 2535–2548 (2010).
7. L. Chou, A. Batchinsky, S. Belenkiy, J. Jing, T. Ramalingam, M. Brenner, and Z. Chen, "In vivo detection of inhalation injury in large airway using three-dimensional long-range swept-source optical coherence tomography," J. Biomed. Opt. **19**(3), 036018 (2014).
8. J. C. Jing, L. Chou, E. Su, B. J. F. Wong, and Z. Chen, "Anatomically correct visualization of the human upper airway using a high-speed long range optical coherence tomography system with an integrated positioning sensor," Sci. Rep. **6**(1), 39443 (2016).
9. Y. Chen, M. Ding, W. J. Guan, W. Wang, W. Z. Luo, C. H. Zhong, M. Jiang, J. H. Jiang, Y. Y. Gu, S. Y. Li, and N. S. Zhong, "Validation of human small airway measurements using endobronchial optical coherence tomography," Respir. Med. **109**(11), 1446–1453 (2015).
10. J. N. S. d'Hooghe, A. W. M. Goorsenberg, D. M. de Bruin, J. J. T. H. Roelofs, J. T. Annema, and P. I. Bonta, "Optical coherence tomography for identification and quantification of human airway wall layers," PLoS One **12**(10), e0184145 (2017).
11. D. C. Adams, Y. Wang, L. P. Hariri, and M. J. Suter, "Advances in Endoscopic Optical Coherence Tomography Catheter Designs," IEEE J. Sel. Top. Quantum Electron. **22**(3), 12 (2016).
12. D. C. Adams and M. J. Suter, "Processing-based approach for resolving the sample optic axis in endoscopic polarization-sensitive optical coherence tomography," Opt. Express **26**(19), 24917–24927 (2018).
13. A. M. D. Lee, K. Ohtani, C. Macaulay, A. McWilliams, T. Shaipanich, V. X. D. Yang, S. Lam, and P. Lane, "In vivo lung microvasculature visualized in three dimensions using fiber-optic color Doppler optical coherence tomography," J. Biomed. Opt. **18**(5), 50501 (2013).
14. H. Pahlevaninezhad, A. M. D. Lee, S. Lam, C. MacAulay, and P. M. Lane, "Coregistered autofluorescence-optical coherence tomography imaging of human lung sections," J. Biomed. Opt. **19**(3), 036022 (2014).
15. H. Pahlevaninezhad, A. M. D. Lee, G. Hohert, S. Lam, T. Shaipanich, E. L. Beaudoin, C. MacAulay, C. Boudoux, and P. Lane, "Endoscopic high-resolution autofluorescence imaging and OCT of pulmonary vascular networks," Opt. Lett. **41**(14), 3209–3212 (2016).
16. L. P. Hariri, M. Villiger, M. B. Applegate, M. Mino-Kenudson, E. J. Mark, B. E. Bouma, and M. J. Suter, "Seeing beyond the Bronchoscope to Increase the Diagnostic Yield of Bronchoscopic Biopsy," Am. J. Respir. Crit. Care Med. **187**(2), 125–129 (2013).
17. J. Li, F. Feroldi, J. de Lange, J. M. A. Daniels, K. Grünberg, and J. F. de Boer, "Polarization sensitive optical frequency domain imaging system for endobronchial imaging," Opt. Express **23**(3), 3390–3402 (2015).
18. L. Wijmans, J. N. d'Hooghe, P. I. Bonta, and J. T. Annema, "Optical coherence tomography and confocal laser endomicroscopy in pulmonary diseases," Curr. Opin. Pulm. Med. **23**(3), 275–283 (2017).
19. P. G. Cox, J. Miller, W. Mitzner, and A. R. Leff, "Radiofrequency ablation of airway smooth muscle for sustained treatment of asthma: preliminary investigations," Eur. Respir. J. **24**(4), 659–663 (2004).

Biomedical Optics EXPRESS

20. C. J. Danek, C. M. Lombard, D. L. Dungworth, P. G. Cox, J. D. Miller, M. J. Biggs, T. M. Keast, B. E. Loomas, W. J. Wizeman, J. C. Hogg, and A. R. Leff, "Reduction in airway hyperresponsiveness to methacholine by the application of RF energy in dogs," J. Appl. Physiol. **97**(5), 1946–1953 (2004).
21. G. Cox, J. D. Miller, A. McWilliams, J. M. Fitzgerald, and S. Lam, "Bronchial thermoplasty for asthma," Am. J. Respir. Crit. Care Med. **173**(9), 965–969 (2006).
22. A. W. M. Goorsenberg, J. N. S. d'Hooghe, D. M. de Bruin, I. A. H. van den Berk, J. T. Annema, and P. I. Bonta, "Bronchial thermoplasty-induced acute airway effects assessed with optical coherence tomography in severe asthma," Respiration **96**(6), 564–570 (2018).
23. B. Baumann, W. Choi, B. Potsaid, D. Huang, J. S. Duker, and J. G. Fujimoto, "Swept source/Fourier domain polarization sensitive optical coherence tomography with a passive polarization delay unit," Opt. Express **20**(9), 10229–10241 (2012).
24. M. Villiger, E. Z. Zhang, S. K. Nadkarni, W.-Y. Oh, B. J. Vakoc, and B. E. Bouma, "Spectral binning for mitigation of polarization mode dispersion artifacts in catheter-based optical frequency domain imaging," Opt. Express **21**(14), 16353–16369 (2013).
25. B. Baumann, E. Götzinger, M. Pircher, H. Sattmann, C. Schuutze, F. Schlanitz, C. Ahlers, U. Schmidt-Erfurth, and C. K. Hitzenberger, "Segmentation and quantification of retinal lesions in age-related macular degeneration using polarization-sensitive optical coherence tomography," J. Biomed. Opt. **15**(6), 061704 (2010).
26. N. Lippok, M. Villiger, and B. E. Bouma, "Degree of polarization (uniformity) and depolarization index: unambiguous depolarization contrast for optical coherence tomography," Opt. Lett. **40**(17), 3954–3957 (2015).
27. S. Makita, Y.-J. Hong, M. Miura, and Y. Yasuno, "Degree of polarization uniformity with high noise immunity using polarization-sensitive optical coherence tomography," Opt. Lett. **39**(24), 6783–6786 (2014).
28. V. Davidoiu, L. Hadjilucas, I. Teh, N. P. Smith, J. E. Schneider, and J. Lee, "Evaluation of noise removal algorithms for imaging and reconstruction of vascular networks using micro-CT," Biomed. Phys. Eng. Express **2**(4), 045015 (2016).
29. E. Z. Zhang, W. Y. Oh, M. L. Villiger, L. Chen, B. E. Bouma, and B. J. Vakoc, "Numerical compensation of system polarization mode dispersion in polarization-sensitive optical coherence tomography," Opt. Express **21**(1), 1163–1180 (2013).
30. B. Braaf, K. A. Vermeer, M. de Groot, K. V. Vienola, and J. F. de Boer, "Fiber-based polarization-sensitive OCT of the human retina with correction of system polarization distortions," Biomed. Opt. Express **5**(8), 2736–2758 (2014).
31. M. G. O. Graefe, J. A. Van de Kreeke, J. Willemse, Y. de Jong, H. S. Tan, F. Verbraak, and J. F. de Boer, "Subretinal Fibrosis Detection using Polarization Sensitive Optical Coherence Tomography," In preparation (2019).
32. M. Villiger, D. Lorenser, R. A. McLaughlin, B. C. Quirk, R. W. Kirk, B. E. Bouma, and D. D. Sampson, "Deep tissue volume imaging of birefringence through fibre-optic needle probes for the delineation of breast tumour," Sci. Rep. **6**(1), 28771 (2016).
33. R. Azzam, "Propagation of partially polarized light through anisotropic media with or without depolarization: a differential 4× 4 matrix calculus," JOSA **68**(12), 1756–1767 (1978).
34. B. H. Park, M. C. Pierce, B. Cense, and J. F. de Boer, "Jones matrix analysis for a polarization-sensitive optical coherence tomography system using fiber-optic components," Opt. Lett. **29**(21), 2512–2514 (2004).
35. J. Willemse, M. G. O. Graefe, J. A. van de Kreeke, F. Feroldi, F. Verbraak, and J. F. de Boer, "Optic axis uniformity as a metric to improve the contrast of birefringent structures and analyze the retinal nerve fiber layer," In preparation (2019).
36. M. Yamanari, K. Ishii, S. Fukuda, Y. Lim, L. Duan, S. Makita, M. Miura, T. Oshika, and Y. Yasuno, "Optical rheology of porcine sclera by birefringence imaging," PLoS One **7**(9), e44026 (2012).
37. Q. Li, K. Karnowski, P. B. Noble, A. Cairncross, A. James, M. Villiger, and D. D. Sampson, "Robust reconstruction of local optic axis orientation with fiber-based polarization-sensitive optical coherence tomography," Biomed. Opt. Express **9**(11), 5437–5455 (2018).
38. M. Villiger, B. Braaf, N. Lippok, K. Otsuka, S. K. Nadkarni, and B. E. Bouma, "Optic axis mapping with catheter-based polarization-sensitive optical coherence tomography," Optica **5**(10), 1329–1337 (2018).
39. C. Sun, F. Nolte, K. H. Y. Cheng, B. Vuong, K. K. C. Lee, B. A. Standish, B. Courtney, T. R. Marotta, A. Mariampillai, and V. X. D. Yang, "In vivo feasibility of endovascular Doppler optical coherence tomography," Biomed. Opt. Express **3**(10), 2600–2610 (2012).
40. O. O. Ahsen, H. C. Lee, M. G. Giacomelli, Z. Wang, K. Liang, T. H. Tsai, B. Potsaid, H. Mashimo, and J. G. Fujimoto, "Correction of rotational distortion for catheter-based en face OCT and OCT angiography," Opt. Lett. **39**(20), 5973–5976 (2014).
41. T. H. Tsai, O. O. Ahsen, H. C. Lee, K. Liang, M. Figueiredo, Y. K. Tao, M. G. Giacomelli, B. M. Potsaid, V. Jayaraman, Q. Huang, A. E. Cable, J. G. Fujimoto, and H. Mashimo, "Endoscopic Optical Coherence Angiography Enables 3-Dimensional Visualization of Subsurface Microvasculature," Gastroenterology **147**(6), 1219–1221 (2014).
42. M. J. Ju, Y.-J. Hong, S. Makita, Y. Lim, K. Kurokawa, L. Duan, M. Miura, S. Tang, and Y. Yasuno, "Advanced multi-contrast Jones matrix optical coherence tomography for Doppler and polarization sensitive imaging," Opt. Express **21**(16), 19412–19436 (2013).

Biomedical Optics EXPRESS

43. B. Braaf, K. A. Vermeer, V. A. Sicam, E. van Zeeburg, J. C. van Meurs, and J. F. de Boer, "Phase-stabilized optical frequency domain imaging at 1-μm for the measurement of blood flow in the human choroid," Opt. Express **19**(21), 20886–20903 (2011).
44. B. Braaf, K. A. Vermeer, K. V. Vienola, and J. F. de Boer, "Angiography of the retina and the choroid with phase-resolved OCT using interval-optimized backstitched B-scans," Opt. Express **20**(18), 20516–20534 (2012).
45. M. Almasian, N. Bosschaart, T. G. van Leeuwen, and D. J. Faber, "Validation of quantitative attenuation and backscattering coefficient measurements by optical coherence tomography in the concentration-dependent and multiple scattering regime," J. Biomed. Opt. **20**(12), 121314 (2015).
46. S. Liu, Y. Sotomi, J. Eggermont, G. Nakazawa, S. Torii, T. Ijichi, Y. Onuma, P. W. Serruys, B. P. F. Lelieveldt, and J. Dijkstra, "Tissue characterization with depth-resolved attenuation coefficient and backscatter term in intravascular optical coherence tomography images," J. Biomed. Opt. **22**(9), 1–16 (2017).
47. S. Stefan, K.-S. Jeong, C. Polucha, N. Tapinos, S. A. Toms, and J. Lee, "Determination of confocal profile and curved focal plane for OCT mapping of the attenuation coefficient," Biomed. Opt. Express **9**(10), 5084–5099 (2018).
48. K. A. Vermeer, J. Mo, J. J. A. Weda, H. G. Lemij, and J. F. de Boer, "Depth-resolved model-based reconstruction of attenuation coefficients in optical coherence tomography," Biomed. Opt. Express **5**(1), 322–337 (2014).
49. H. Pahlevaninezhad, A. M. D. Lee, A. Ritchie, T. Shaipanich, W. Zhang, D. N. Ionescu, G. Hohert, C. MacAulay, S. Lam, and P. Lane, "Endoscopic Doppler optical coherence tomography and autofluorescence imaging of peripheral pulmonary nodules and vasculature," Biomed. Opt. Express **6**(10), 4191–4199 (2015).
50. F. Feroldi, M. Verlaan, H. Knaus, V. Davidoiu, D. J. Vugts, G. A. M. S. van Dongen, C. F. M. Molthoff, and J. F. de Boer, "High resolution combined molecular and structural optical imaging of colorectal cancer in a xenograft mouse model," Biomed. Opt. Express **9**(12), 6186–6204 (2018).